



A Robust Two-Degree-of-Freedom Current Control Strategy for *LCL*-Equipped High-Speed PMSMs

Journal:	<i>IEEE Transactions on Power Electronics</i>
Manuscript ID:	TPEL-Reg-2024-01-0007
Manuscript Type:	Regular Paper (S1)
Date Submitted by the Author:	02-Jan-2024
Complete List of Authors:	Shi, Longhao; Southeast University, Cheng, Chenwen; Southeast University, Hu, Mingjin; Southeast University, Hua, Wei; School of Electrical Engineering, Southeast University, Lu, Chunyu; Southeast University
Keywords:	Active damping, Digital control, AC motor drives, Passive filters

SCHOLARONE™
Manuscripts

> REPLACE THIS LINE WITH YOUR MANUSCRIPT ID NUMBER (DOUBLE-CLICK HERE TO EDIT) <

A Robust Two-Degree-of-Freedom Current Control Strategy for *LCL*-Equipped High-Speed PMSMs

Longhao Shi, Chenwen Cheng, Mingjin Hu, *Student Member, IEEE*, Wei Hua, *Senior Member, IEEE*, Chunyu Lu

Abstract—For an inductor-capacitor-inductor (*LCL*) equipped high-speed permanent magnet synchronous machine (*LCL-HSPMSM*), the negative resonance frequency in the synchronous rotating frame will impact the robustness of the adjustable-speed system, which has barely been assessed. This paper proposes a two-degree-of-freedom (2DOF) current control strategy, which achieves strong robustness by maximizing the global stability margin. Firstly, a mathematical model of an *LCL-HSPMSM* in the discrete-time domain is established, based on which the influence of both positive and negative resonance frequencies on the system stability is analyzed. Secondly, a novel 2DOF control strategy for the *LCL-HSPMSM* with motor current feedback only is proposed, which introduces a phase gain to achieve the maximum global stability margin. An additional DOF is provided by a feedforward controller to reduce the coupling between *dq*-axes currents, which is different from the normal control strategy. Thus, a strong robustness against parameter mismatches can be achieved and the parameter determination procedure of the robust control strategy is described in detail. Finally, experimental verification of the robust control strategy is conducted on a 60kr/min *LCL-HSPMSM* prototype, where key parameters are varied from 0.3 to 3 times of the nominal values.

Index Terms—*LCL* filter, HSPMSM, robustness, discrete time, synchronous rotating frame, complex vector, feedforward.

I. INTRODUCTION

HIGH-SPEED surface-mounted permanent magnet synchronous motors (HSPMSMs) are extensively employed in industrial applications due to their remarkable power density and efficiency. However, the small motor inductance results in significant current ripples, leading to additional power losses and torque ripples. To address this issue, an *LCL* filter can be implemented between the inverter and the motor as shown in Fig. 1. Nevertheless, the high-order nature of the *LCL* filter significantly increases system complexity, posing challenges for the controller design. In particular, the resonance peak introduced by the *LCL* circuit potentially affects the stability of the current control loop [1], [2]. Moreover, the system parameters vary widely in different operating conditions, demanding strong parameters robustness for the controller design.

The next few paragraphs should contain the authors' current affiliations, including current address and e-mail. For example, First A. Author is with the National Institute of Standards and Technology, Boulder, CO 80305 USA (e-mail: author@boulder.nist.gov).

Second B. Author Jr. was with Rice University, Houston, TX 77005 USA. He is now with the Department of Physics, Colorado State University, Fort Collins, CO 80523 USA (e-mail: author@lamar.colostate.edu).

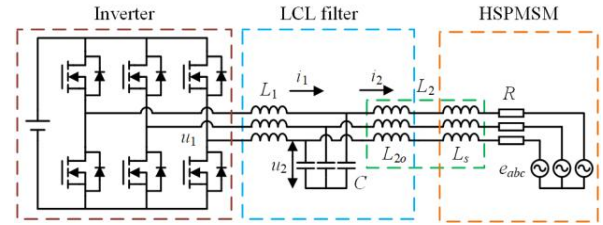


Fig. 1 System diagram of the *LCL-HSPMSM* system.

Considerable research efforts have been dedicated to the development of active damping (AD) strategies to effectively address the resonance issue, which can be concluded as resonant pole cancellation [3]–[6], virtual-resistance [7]–[11], full-state feedback control (FSFC) [12]–[16], and filter-based damping [17]–[20].

Resonant pole cancellation methods include the notch filter [3], weighted average current (WAC) control [4], and capacitor voltage feedback [5]. A cascade notch filter is a straightforward method to cancellate the resonance pole by setting the notch frequency exactly at the resonance frequency. The resonant pole can also be cancelled by the reasonable configuration of weight facts of WAC or capacitor feedback coefficient. However, these methods require the exact value of resonance frequency, when parameter mismatch occurs, the damping effects will deteriorate seriously, indicating weak robustness [6].

The virtual-resistance AD method is popularly used, which is mainly achieved by the proportional capacitor current feedback [7], [8]. However, the effectiveness of this method is highly degraded by the inherent digital computation delay. To address this issue, some improvements were employed by reducing computational delay [9] or modifying the feedback strategy [10], [11]. Nevertheless, the robustness is still limited by the digital delay, and the requirement for the additional capacitor current measurement leads to extra costs.

The FSFC method can achieve robustness through arbitrary pole assignment [12], [13]. However, this approach necessitates the costly measurement of all states. Introducing a state observer allows for the implementation of full state feedback with just a single sensor [14], [15]. Furthermore, a single-sensor damping framework is introduced, enabling equivalent arbitrary pole assignment with a single sensor without the need for an observer [16], [21]. Nevertheless, these methods heavily rely on system parameters, and parameter mismatch can degrade the system's robustness, especially with a state observer.

The filter-based damping methods seem to be a proper way to achieve high parameters robustness because the controller

> REPLACE THIS LINE WITH YOUR MANUSCRIPT ID NUMBER (DOUBLE-CLICK HERE TO EDIT) <

design is relatively insensitive to the system parameters. For the motor side current or grid side current feedback system, the resonance is damped by introducing an additional phase lag in the resonance frequency. Various methods are employed to achieve this goal, including the use of first-order low-pass filters (LPF), second-order LPF [17], and the introduction of additional delay [18]. Additionally, the notch filter can also serve as an LPF due to its phase lag characteristic to the left of the notch frequency [19].

Overall, the aforementioned methods are mostly established in the stationary coordinate for grid-connected applications. For the *LCL*-HSPMSM system, the motor current controller is usually designed in the synchronous rotating frame to improve the current transient performance. In previous studies, a dynamic decoupled controller with a notch filter damping was introduced to achieve dynamic decoupling [20]. However, a potential negative resonance frequency in the rotating frame is ignored in this method, which may lead to instability issues. Thus, the robustness of this method is also limited.

This paper conducts a comprehensive analysis of the influence of the negative resonance frequency and proposes a 2DOF control strategy within the synchronous rotating frame to ensure global stability. The main contributions of this article can be summarized as follows:

- 1) A more appropriate indicator considering both negative and positive frequency domains is proposed for assessing the global stability margin.
- 2) A phase gain is introduced to enhance the global stability, thus achieving strong robustness with varying system parameters.
- 3) The coupling effects of currents in *dq*-axes are addressed by an additional DOF provided by a feedforward controller.

Finally, the effectiveness of the proposed control strategy is validated by driving the test HSPMSM up to 60 kr/min (1000Hz) with a sampling frequency of 15kHz. The robustness is validated in the experiment with all the system parameters varying from 0.3 to 3 times their nominal values.

TABLE I
CRITICAL PARAMETERS OF THE *LCL*-HSPMSM

Symbol	Parameter	Value
<i>R</i>	winding resistance	0.02Ω
<i>L</i> ₁	inductance at the inverter side	60uH
<i>L</i> _{2o}	inductance at the machine side	50uH
<i>L</i> _s	inductance of the machine	11uH
<i>C</i>	capacitor of <i>LCL</i> filter	60μF
<i>f</i> _{res}	resonance frequency	3736Hz
<i>U</i> _{dc}	DC bus voltage	60V
<i>f</i> _s	sampling frequency	15kHz
<i>f</i> _{sw}	switching frequency	15kHz
<i>ψ</i> _r	flux linkage	1.02mWb
<i>P</i> _r	pole pairs	1
<i>n</i> _N	rated speed	60000rpm
<i>f</i> _e	rated electrical frequency	1000Hz

II. STABILITY ANALYSIS BASED ON DISCRETE TIME MODEL

This section will model the *LCL*-HSPMSM system in the discrete-time domain. The diagram of the system is depicted in Fig. 1, comprising a three-phase inverter, an *LCL* filter, and an HSPMSM. The inverter side inductor is defined as *L*₁. The filter capacitor is defined as *C*. And the motor side inductor is defined as *L*₂, which consists of the filter inductor *L*_{2o} and the motor inductor *L*_s. *R* is the winding resistance. All the parameters are outlined in TABLE I, and these parameters are utilized in the analysis presented in this paper as well as in the conducted experiments in section VI.

A. Discrete Model

The continuous-time transfer function of the motor current in the *αβ* stationary coordinate is derived as

$$G_{ps}(s) = \frac{i_2(s)}{u_1(s)} = \frac{1}{R + (L_1 + L_2)s + L_1 C R s^2 + L_1 L_2 C s^3} \quad (1)$$

Accurate modeling of the *LCL*-equipped HSPMSM system is essential for the current controller design. The transformation of the physical system in the discrete domain can be accomplished by using the zero-order hold method. However, due to the complexity of discretization results, the resistors are typically ignored in the previous studies [22], [23]. This paper introduces an approximate discretization method that yields a relatively simplified model to achieve a more precise discrete model that takes *R*_s into account.

First, the transfer function *G*_{ps}(*s*) in the continuous domain can be approximately divided into the low-frequency and high-frequency components, which are given by

$$G_{ps}(s) \approx G_{psl}(s) + G_{psh}(s) \quad (2)$$

$$G_{psl}(s) = \frac{1}{R + (L_1 + L_2)s}, \quad G_{psh}(s) = -\frac{1}{L_1 + L_2} \frac{s}{s^2 + \omega_{res}^2}$$

where *G*_{psl}(*s*), *G*_{psh}(*s*) is the low-frequency and high-frequency components, and $\omega_{res} = 2\pi f_{res} = \sqrt{(L_1 + L_2)/(L_1 L_2 C)}$ is the natural resonance frequency. Compared with the previous model (*G*_{psl}(*s*)=1/(*L*₁+*L*₂)*s*) [19], the proposed model preserves a more accurate pole in the low frequency by considering the winding resistance in *G*_{psl}(*s*).

By discretizing the separated model with the zero-order hold method, an accurate model with delay can be obtained by

$$G_{ps}(z) = z^{-1} (G_{psl}(z) + G_{psh}(z)) \quad (3)$$

where

$$G_{psl}(z) = \frac{1 - e^{-\frac{R}{L_1 + L_2} T_s}}{R} \frac{1}{z - e^{-\frac{R}{L_1 + L_2} T}} \quad (4)$$

$$G_{psh}(z) = -\frac{(z-1)\sin(\omega_{res} T)}{\omega_{res} (L_1 + L_2)(z^2 - 2z \cos(\omega_{res} T) + 1)}$$

Further, the transfer function *G*_p(*z*) in the synchronous rotating frame can be developed by applying the frequency shift $z \rightarrow ze^{j\omega_e T}$, which leads to

$$G_p(z) = z^{-1} e^{-j\omega_e T} (G_{pl}(z) + G_{ph}(z)) \quad (5)$$

where

> REPLACE THIS LINE WITH YOUR MANUSCRIPT ID NUMBER (DOUBLE-CLICK HERE TO EDIT) <

$$G_{pl}(z) = \frac{1 - e^{-\frac{R}{L_1 + L_2}T_s}}{R} \frac{1}{ze^{j\omega_e T} - e^{-\frac{R}{L_1 + L_2}T}} \quad (6)$$

$$G_{ph}(z) = -\frac{(ze^{j\omega_e T} - 1)\sin(\omega_{res} T)}{\omega_{res}(L_1 + L_2)(z^2 e^{2j\omega_e T} - 2ze^{j\omega_e T} \cos(\omega_{res} T) + 1)}$$

Notably, since the amplitude of the two transfer functions in their respective frequency bands is much larger than that of the other as shown in Fig. 2, they can be discussed separately in the design of the controller.

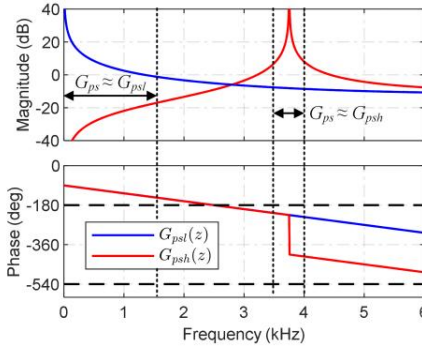


Fig. 2 Bode diagram of $G_{pst}(z)$ and $G_{psh}(z)$.

B. Stabilities in Positive and Negative Frequency Domains

In the existing studies, the stability of *LCL* system is typically proved by the Nyquist stability criterion based on the Bode diagram. Due to the symmetry of the real system's transfer function in both positive and negative frequency domains, it is typically sufficient to focus on the positive frequency domain.

However, in the rotating coordinates, the transfer function in (6) contains complex coefficients, which violates the symmetry in the frequency domain. And this problem is especially critical under high-speed conditions because of the larger resonance frequency shift.

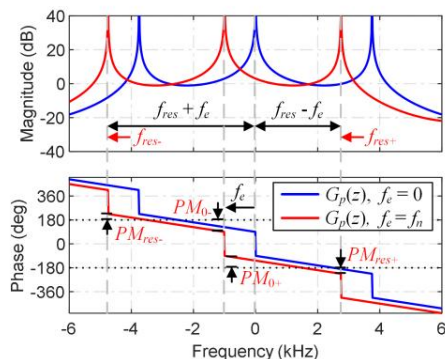


Fig. 3 Bode diagram of both positive and negative frequency domain with speed variation.

Fig. 3 shows the bode diagram variation with electric frequency f_e . As f_e increases, the bode plots shift to the left and lose its symmetry. Therefore, in the *dq* axis, there are two different resonant frequencies: $f_{res+} = f_{res} - f_e$ and $f_{res-} = f_{res} + f_e$.

According to the Nyquist stability criterion, the system is stable when no phase response crosses the $(2k-1)\pi$ phase line

at both resonant frequencies.

For the positive and negative resonant frequencies combined with two 0dB crossing frequencies around the fundamental frequency band, the instability can occur at any of these frequencies if a crossing occurs.

Thus, considering parameter robustness, four types of phase margins (*PMs*) are introduced to describe the system stability margin, which is defined as:

- 1) PM_{0+} : *PM* at positive 0dB crossing frequency.
- 2) PM_{0-} : *PM* at negative 0dB crossing frequency.
- 3) PM_{res+} : *PM* at positive resonance frequency.
- 4) PM_{res-} : *PM* at negative resonance frequency.

All of the above *PMs* are illustrated in Fig. 3. Among these four *PM* values, a low value for any of them would lead to a decrease in the system's stability margin, resulting in a deterioration of stability and control performance.

Thus, the global phase margin is defined as

$$PM_{min} = \min\{PM_{0-}, PM_{0+}, PM_{-}, PM_{+}\} \quad (7)$$

The *PM* of the low frequency and resonance frequency band can be respectively defined as

$$\begin{aligned} PM_0 &= \min\{PM_{0-}, PM_{0+}\} \\ PM_{res} &= \min\{PM_{res-}, PM_{res+}\} \end{aligned} \quad (8)$$

PM_{min} is a more concise metric to represent the global stability margin of the system, and the method to achieve the maximum PM_{min} will be analyzed in detail in this paper.

C. Limitations of Existing Damping Methods

In the synchronous rotating frame, the potential negative frequency is nonnegligible. Consequently, certain existing damping methods may render the system unstable when designed in the *dq* axis.

Fig. 4 shows the bode diagram of the existing damping methods designed in the synchronous rotating frame, including a notch filter [19] and an additional delay [18].

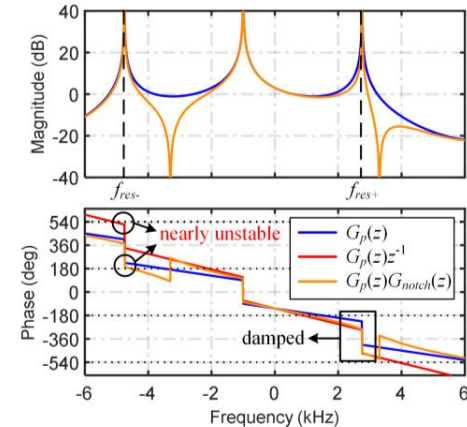


Fig. 4 Bode diagram of existing damping methods.

Firstly, in terms of damping methods with an additional delay, it could introduce a phase lag in f_{res+} , thus effectively damping the resonance. However, simultaneously, the additional delay introduces a considerably greater phase lead in f_{res-} within the negative frequency domain, potentially causing system instability.

> REPLACE THIS LINE WITH YOUR MANUSCRIPT ID NUMBER (DOUBLE-CLICK HERE TO EDIT) <

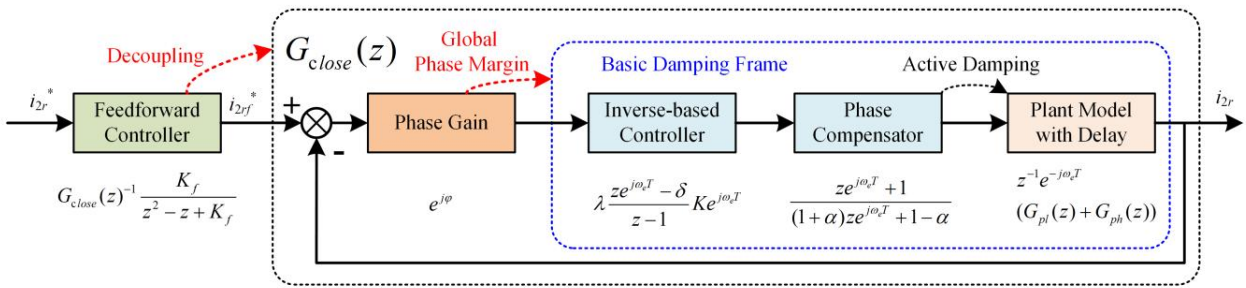


Fig. 5 Block diagram of the proposed 2DOF current control strategy.

Similarly, if a notch filter is introduced to add extra phase lag in the positive resonance frequency f_{res+} , there is an almost 180° crossing in the negative frequency f_{res-} due to the phase lead effects of the notch filter when the frequency surpasses the notch frequency.

In conclusion, PM_{min} of both damping methods are very small, indicating a weak robustness of the system.

To address these challenges, this paper proposes a novel current control strategy with a phase compensator designed in the stationary coordinate frame, accompanied by additional damping and decoupling methods, which will be further discussed in section III.

III. PROPOSED CURRENT CONTROL STRATEGY

In this section, a robust 2DOF current control strategy is proposed as shown in Fig. 5, including three parts:

- 1) Basic damping frame consists of an inverse-based controller and a phase compensator.
- 2) A phase gain to provide a global stability margin.
- 3) A feedforward controller to decouple the dynamic response of the dq -axes currents, introducing an additional DOF.

The design concept of the proposed method is to ensure sufficient stability margin within the closed-loop system and achieve decoupling through the inversion of the closed-loop transfer function in the feedforward decoupling controller.

A. Basic Damping Frame

The basic damping frame of the proposed strategy consists of an inverse-based controller and a phase compensator.

Firstly, in II.A, it has been proved that the plant model G_p can be simplified as G_{pl} in low frequency. It means the LCL system can be simplified as a first-order motor model in low-frequency band. Thus, the inverse-based controller is introduced to cancellate the first-order pole in the low frequency band, which is given as

$$G_{inv}(z) = (G_{pl}(z)z^{-1}e^{-j\omega_e T})^{-1} \frac{K}{z(z-1)} = \lambda \frac{ze^{j\omega_e T} - \delta}{z-1} K e^{j\omega_e T} \quad (9)$$

where

$$\delta = e^{-\frac{R}{L_1 + L_2} T}, \quad \lambda = \frac{R}{1 - e^{-\frac{R}{L_1 + L_2} T_s}} \quad (10)$$

and K is the closed-loop gain of the system.

The inverse-based controller can be considered as a PI

controller designed in discrete domain with an angel delay compensation. It outperforms any other form of the PI controller for the first-order motor model [24].

Secondly, the phase compensator designed in the stationary frame is introduced to perform active damping for resonance effects. The phase compensator is derived from the first-order LPF with discretization method of pre-twisted bilinear transformation, for its capability to keep the phase characteristics at the resonance frequency unchanged [25], which is derived as

$$\begin{aligned} G_{pc}(z) &= \frac{\omega_{lpf}}{s + \omega_{lpf}} \left(s = \frac{\omega_{res}}{\tan(\frac{\omega_{res}T}{2})} \frac{z-1}{z+1} \right) \\ &= \frac{z+1}{(1+\alpha)z+1-\alpha} \left(\alpha = \frac{\omega_{res}}{\omega_{lpf} \tan(\frac{\omega_{res}T}{2})} \right). \end{aligned} \quad (11)$$

The equivalent transfer function in the rotating frame is given as

$$G_{pc}(z) = G_{pc}(ze^{j\omega_e T}) = \frac{ze^{j\omega_e T} + 1}{(1+\alpha)ze^{j\omega_e T} + 1 - \alpha}. \quad (12)$$

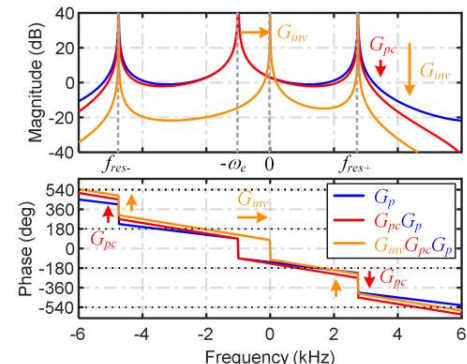


Fig. 6 Bode diagram of basic damping frame.

The effects of the inverse-based controller and the phase compensator are illustrated in Fig. 6. The phase compensator reduces the phase in f_{res+} and increases the phase in f_{res-} . Thus, the active damping of resonance is achieved by keeping the phase at both resonance frequency away from the $(2k-1)\pi$ phase line. As a result, the global phase margin can be increased.

Further, the inverse-based controller shifts the speed coupled pole $-\omega_e$ to 0Hz and greatly reduces the magnitude in the high

> REPLACE THIS LINE WITH YOUR MANUSCRIPT ID NUMBER (DOUBLE-CLICK HERE TO EDIT) <

frequency band. Thus, an infinite gain in 0Hz is achieved to completely eliminate steady-state errors. And the resonance effects are well damped due to low magnitude in the resonance frequency.

B. Phase Gain

On the basis of the phase compensator, the global phase margin of the system can be further enhanced by introducing a series phase gain, which is given as

$$G_{pg}(z) = e^{j\varphi} \quad (13)$$

where φ is the global phase shift angle.

The effects of phase gain are shown in Fig. 7. When φ is negative, the phase-frequency curve shifts downward as a whole. It can be found that as the phase gain decreases, PM_{res} increases, while PM_0 decreases. As PM_{min} is determined by the minimum phase margin among all components, by reasonably setting the phase gain, it is possible to ensure that PM_0 and PM_{res} remain identical, thereby maximizing the global system margin.

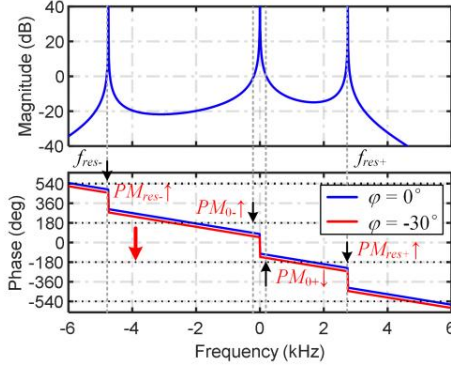


Fig. 7 Effects of phase gain.

C. Feedforward Decoupling Controller

In the above design, the additional phase compensator and phase gain are all complex vector controllers, which will cause additional coupling effects [26]. Therefore, a feedforward decoupling controller is proposed to achieve dynamic decoupling by inverting the closed-loop transfer function of the system. The specific expression is as follows

$$\begin{aligned} G_{ff}(z) &= G_{close}^{-1}(z) \frac{K_f}{z^2 - z + K_f} \\ &= \frac{1 + G_{pg}(z)G_{inv}(z)G_{pc}(z)G_p(z)}{G_{pg}(z)G_{inv}(z)G_{pc}(z)G_p(z)} \frac{K_f}{z^2 - z + K_f} \\ &= \frac{K_f}{K} e^{-j\varphi} ((1+\alpha) + ((1-\alpha)e^{-j\omega_e T} - (1+\alpha))z^{-1} \\ &\quad + ((\alpha-1)e^{-j\omega_e T} + Ke^{j\varphi})z^{-2} + Ke^{j\varphi-j\omega_e T}z^{-3}) / \\ &\quad (1 + (e^{-j\omega_e T} - 1)z^{-1} + (K_f - e^{-j\omega_e T})z^{-2} + K_f e^{-j\omega_e T}z^{-3}) \end{aligned} \quad (14)$$

where K_f represents the feedforward gain of the system.

IV. PARAMETER DETERMINATION PROCEDURE

This section introduces the parameter design procedure for the proposed control strategy, aiming at maximizing the

stability margin while ensuring dynamic performance. It should be emphasized that, unlike the general controller design methods, the following analysis simultaneously considers the aforementioned four PMs to guarantee system stability against significant parameter variations at high speeds.

A. Phase Compensator

The phase compensator is designed to lag the phase mutation at the resonance frequency to between -180° and -540° . In the following, the phase of $G_{ps}(z)$ at the resonance frequency is firstly calculated, and accordingly, the coefficients α of the phase compensator is further determined.

As aforementioned, at the resonance frequency, the amplitude of the low-frequency transfer function is negligible. So the phase at the resonance frequency can be directly obtained based on the high-frequency transfer function, which is given as

$$\begin{aligned} \angle G_{ps}(e^{j\omega_{res}T})(\omega \rightarrow \omega_{res}-) \\ = \arctan 2(\sin(\omega_{res}T), \cos(\omega_{res}T)-1) - 2\omega_{res}T - \pi \\ \angle G_{ps}(e^{j\omega_{res}T})(\omega \rightarrow \omega_{res}+) \\ = \arctan 2(\sin(\omega_{res}T), \cos(\omega_{res}T)-1) - 2\omega_{res}T - 2\pi \end{aligned} \quad (15)$$

The design objective of the phase compensator is to control the phase shift to be from -1.5π to -2.5π . Thus, the phase lag to be compensated is calculated as

$$\begin{aligned} \varphi_{pc} &= \angle G_{pc}(z)(z = e^{j\omega_{res}T}) \\ &= -\arctan 2(\sin(\omega_{res}T), \cos(\omega_{res}T)-1) + 2\omega_{res}T - \frac{\pi}{2} \end{aligned} \quad (16)$$

Next, based on the required phase shift, the bandwidth of the first-order low-pass filter is calculated as

$$\omega_{lpf} = \omega_{res} / \tan(\varphi_{pc}) \quad (17)$$

And the corresponding discrete domain transfer function coefficients can be calculated as

$$\alpha = \frac{\omega_{res}}{\omega_{lpf} \tan(\frac{\omega_{res}T}{2})} = \frac{\tan(\varphi_{pc})}{\tan(\frac{\omega_{res}T}{2})} \quad (18)$$

B. Feedforward Gain and closed-loop gain

The gain of the system determines its bandwidth and further affects system stability, dynamic performance, and anti-disturbance performance. This section will discuss the selection of closed-loop gain and feedforward gain from these aspects.

Ignoring the influence of phase compensator and high-frequency resonance, the closed-loop transfer function and follow-up response transfer function of the system can be expressed as

$$G_{close}(z) = \frac{i(z)}{i_{ff}^*(z)} = \frac{K}{z^2 - z + K} \quad (19)$$

$$G_{ref}(z) = \frac{i(z)}{i^*(z)} = \frac{K_f}{z^2 - z + K_f}. \quad (20)$$

Equation (20) indicates that the following response of the

> REPLACE THIS LINE WITH YOUR MANUSCRIPT ID NUMBER (DOUBLE-CLICK HERE TO EDIT) <

system is only related to the feedforward gain K_f . By increasing K_f , the dynamic response of the system can be effectively improved. However, an excessively large feedforward gain makes system more susceptible to the influence of voltage saturation, leading to issues such as overshooting and coupling.

On the other hand, the closed-loop gain K determines the bandwidth of the closed-loop system, and further affects PM_0 . Specifically, the larger K , the lower PM . At the same time, it also increases the amplitude at the resonance frequency, expanding the frequency range above the 0dB line and reducing the stability margin.

For reference, ignoring the effects of phase compensator, the 0dB crossing frequency can be approximately simplified as

$$\omega_{b\text{-close}} \approx \frac{K}{T} \quad (21)$$

In summary, considering the system stability and dynamic performance, the recommended values for the feedforward gain and feedback gain are

$$K = 0.05, K_f = 0.1 \quad (22)$$

In practical applications, corresponding adjustments can be made according to requirements.

C. Phase Gain

In this section, numerical calculation of four phase margins will be performed, including PM_{0+} , PM_0 , PM_{res+} , PM_{res-} . And the effects of the phase gain to maximize the global system margin will be explained in detail.

1) The phase margin in the low-frequency band

In the low frequency band, the open-loop transfer function can be simplified as

$$\begin{aligned} G_l(z) &= G_{inv}(z)G_p(z)G_{pc}(z) \\ &\approx G_{inv}(z)z^{-1}e^{-j\omega_e T}G_{pl}(z)G_{pc}(z) \\ &\approx \frac{K}{z^2 - z} \frac{ze^{j\omega_e T} + 1}{(1 + \alpha)ze^{j\omega_e T} + 1 - \alpha} \end{aligned} \quad (23)$$

where

$$\angle G_{pc}(z)(z = e^{j\omega_e T}) = -\frac{\pi}{2} - \frac{3}{2}\omega_e T \quad (24)$$

The phase of phase compensator can be approximately linearized as

$$\angle G_{pc}(z)(z = e^{j\omega_e T}) \approx -(\omega_e + \omega_e)\frac{\varphi_{pc}}{\omega_{res}} \quad (25)$$

Thus, PM_0 can be calculated as

$$PM_{0+} = \frac{\pi}{2} - \frac{3}{2}\omega_b T - \frac{\omega_b}{\omega_{res}}\varphi_{pc} - \frac{\omega_e}{\omega_{res}}\varphi_{pc} + \varphi \quad (26)$$

$$PM_{0-} = \frac{\pi}{2} - \frac{3}{2}\omega_b T - \frac{\omega_b}{\omega_{res}}\varphi_{pc} + \frac{\omega_e}{\omega_{res}}\varphi_{pc} - \varphi \quad (27)$$

The phase margin in low frequency band is calculated as

$$PM_0 = \frac{\pi}{2} - \frac{3}{2}\omega_b T - \frac{\omega_b}{\omega_{res}}\varphi_{pc} - |\varphi - \frac{\omega_e}{\omega_{res}}\varphi_{pc}| \quad (28)$$

2) The phase margin in the high-frequency band

In high-frequency band, the open-loop transfer function can be simplified as

$$G_l(z) \approx G_{inv}(z)G_{pc}(z)z^{-1}e^{-j\omega_e T}G_{ph}(z) \quad (29)$$

As aforementioned about phase compensator, the phase of plant model series with phase compensator is

$$\begin{aligned} \angle G_p(z)G_{pc}(z)(z = e^{j\omega_{res} T}) &= -\frac{3}{2}\pi \\ \angle G_p(z)G_{pc}(z)(z = e^{j\omega_{res+} T}) &= -\frac{5}{2}\pi \end{aligned} \quad (30)$$

Considering that δ is generally close to 1. The inverse-based controller can be simplified as

$$G_{inv}(z) \approx \lambda K \frac{e^{j(\omega_e + \omega_e)T} - 1}{e^{j\omega_e T} - 1} Ke^{j\omega_e T} \quad (31)$$

And the phase can be calculated as

$$G_{inv}(z)(z = e^{j\omega_{res} T}) \approx \frac{3}{2}\omega_e T, G_{inv}(z)(z = e^{-j\omega_e T}) \approx -\frac{3}{2}\omega_e T \quad (32)$$

Thus, the phase margin in high frequency band is introduced as

$$PM_{res} = PM_{res+} = PM_{res-} = \frac{\pi}{2} - \frac{3}{2}\omega_e T - \varphi \quad (33)$$

The total phase margin of resonance frequency is

$$PM_{res} = \min\{PM_{res+}, PM_{res-}\} = \frac{\pi}{2} - \frac{3}{2}\omega_e T - \varphi \quad (34)$$

3) The global phase margin and phase gain determination

Based on the previous calculations in (28) and (34), the effect of phase gain can be concluded as

$$\begin{aligned} \varphi < \frac{\varphi_{pc}}{\omega_{res}}\omega_e, \varphi \uparrow, PM_0 \uparrow, PM_{res} \downarrow \\ \varphi > \frac{\varphi_{pc}}{\omega_{res}}\omega_e, \varphi \uparrow, PM_0 \downarrow, PM_{res} \downarrow \end{aligned} \quad (35)$$

Thus, the PM in both frequency band can be expressed as

$$\begin{aligned} PM_0 = PM_{0+} &= \frac{\pi}{2} - \frac{3}{2}\omega_b T - \frac{\omega_b}{\omega_{res}}\varphi_{pc} - \frac{\omega_e}{\omega_{res}}\varphi_{pc} + \varphi \\ PM_{res} &= \frac{\pi}{2} - \frac{3}{2}\omega_e T - \varphi \quad (\varphi \leq \frac{\omega_e}{\omega_{res}}\varphi_{pc}). \end{aligned} \quad (36)$$

To achieve the maximum phase margin, the phase gain is selected as

$$\varphi = \begin{cases} \frac{\omega_e}{\omega_{res}}\varphi_{pc}, \omega_e < \omega_b \\ -\frac{3}{4}\omega_e T + \frac{3}{4}\omega_b T + \frac{\omega_b}{2\omega_{res}}\varphi_{pc} + \frac{\omega_e}{2\omega_{res}}\varphi_{pc}, \omega_e > \omega_b \end{cases} \quad (37)$$

And the global phase margin is calculated as

$$PM_{min} = \begin{cases} \frac{\pi}{2} - \frac{3}{2}\omega_b T - \frac{\omega_b}{\omega_{res}}\varphi_{pc}, \omega_e < \omega_b \\ \frac{\pi}{2} - (\omega_e + \omega_b)(\frac{3}{4}T + \frac{\varphi_{pc}}{\omega_{res}}), \omega_e > \omega_b \end{cases} \quad (38)$$

In conclusion, the global phase margin is determined by the electrical frequency and the closed-loop bandwidth. In low-speed area ($\omega_e < \omega_b$), PM_{res} is larger than PM_0 , the global phase

> REPLACE THIS LINE WITH YOUR MANUSCRIPT ID NUMBER (DOUBLE-CLICK HERE TO EDIT) <

margin depends on PM_0 . As the speed increases, PM_{res} gradually decreases. When $\omega_e > \omega_b$, PM_{res} is smaller than PM_0 . Under the effects of the phase gain, the balance of PM_{res} and PM_0 can be achieved.

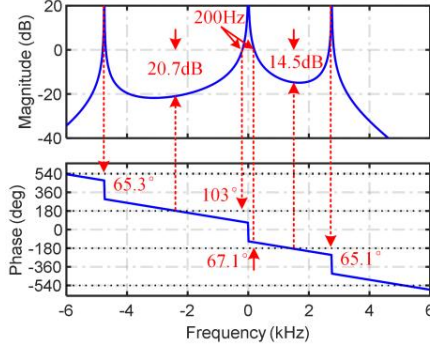


Fig. 8 Bode plots of the designed system ($f_e = 1\text{kHz}$, $f_s = 15\text{kHz}$).

D. Design Results

To further validate the theoretical analysis of parameter selection, a Bode diagram of the designed open-loop system was drawn in Fig. 8. From the graph, it can be seen that the algorithm proposed in this paper can maintain all phase margins of the system above 65° with the gain margin to be 14.5dB at 1000Hz electrical frequency and 200Hz 0dB crossover frequency, which is consistent with the previous analysis and further indicates the strong robustness of the proposed control strategy.

V. ROBUSTNESS ANALYSIS

A. Parameter sensitivity of the closed-loop stability.

The pole maps of the closed-loop system with the plant parameters L_1 , L_2 , C , and R varying from 0.3 to 3 times of their calibrated values are depicted in Fig. 9, with f_e at 1000Hz .

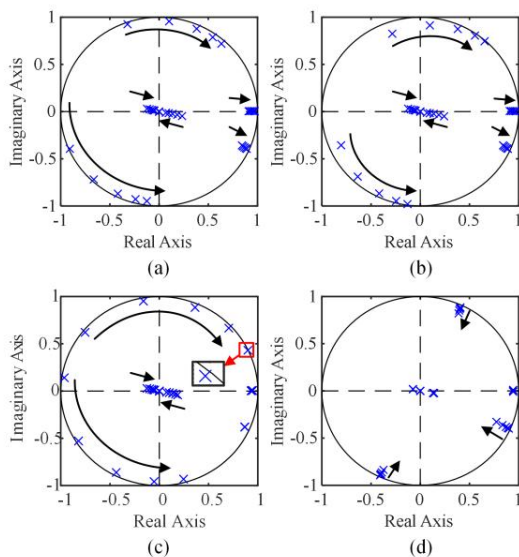


Fig. 9 Pole maps of the closed-loop system with the plant parameter L_1 , L_2 , C and R varying from 30% to 300% with f_e to be 1000Hz . (a) $0.3L_1$ to $3L_1$. (b) $0.3L_2$ to $3L_2$. (c) $0.3C$ to $3C$. (d) $0.3R$ to $3R$.

It is evident that all the closed-loop poles remain within the unit circle, signifying system stability even amidst significant variations in parameters. Notably, the trends in parameter variations appear similar for L_1 , L_2 , and C , whereas the system's stability is notably more sensitive to variations in L_2 and C , since the system is nearly unstable with $3C$ or $3L_2$. Conversely, as R increases, the poles gradually converge towards the center of the unit circle, owing to the damping effect that R imparts to the resonance.

B. Root locus

The pole maps of the closed-loop transfer function with the closed-loop gain K varying from 0.05 to 0.45 are depicted in Fig. 10. As K increases, poles p_1 and p_4 gradually converge towards the center of the unit circle, while poles p_2 and p_3 gradually move from the center to the outside of the circle. All poles strictly remain within the unit circle. The system's stability is primarily determined by p_5 , which moves towards the center and then progressively shifts outward as K exceeds 0.2. The pole reaches outside the unit circle when $K = 0.45$, indicating a critical value of K at 0.4.

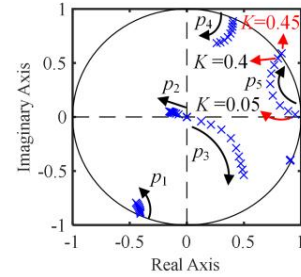


Fig. 10 Root locus with K varying from 0.05 to 0.45.

VI. EXPERIMENT VALIDATION

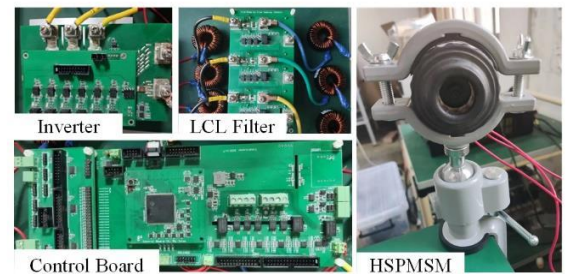


Fig. 11 Schematic diagram of experimental setup.

To validate the effectiveness of the proposed method, an experimental setup was built as shown in Fig. 11. An HSPMSM designed for vacuum cleaners is utilized as the test motor, with its load being directly proportional to the square of the rotational speed. Two three-phase inductors are connected to the AC sampling board in series with the capacitors at the base of the sampling board, forming the *LCL* filter. The control algorithm is executed on a control board based on Texas Instruments high-performance MCU (TMS320F28379D).

The dynamic performance, steady-state performance, decoupling performance and parameter robustness of the

> REPLACE THIS LINE WITH YOUR MANUSCRIPT ID NUMBER (DOUBLE-CLICK HERE TO EDIT) <

system are verified in this section. The parameters of the experimental plant are shown in TABLE I.

A. Steady Performance

In Fig. 12, a current step from 1A to 20A in the i_{2q} reference was executed, with the motor speed rising from 7.36 kr/min (123 Hz) to 62 kr/min (1030 Hz). The results demonstrate the effective damping effects of the proposed method across a wide speed range.

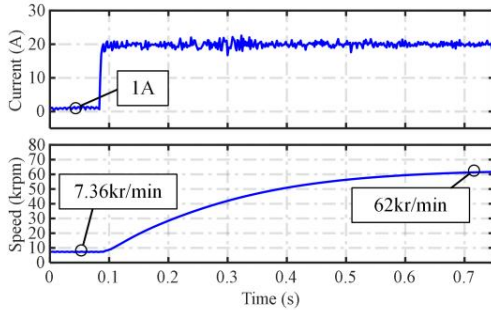


Fig. 12 Steady performance of i_{2q} with different speed.

B. Dynamic Performance with Gain Variation

The dynamic performances with different feedforward gain K_f and closed-loop gain K are illustrated in Fig. 13.

Notably, the dynamic performance is assessed through a current step of i_{2q} from 20A to 30A and a subsequent step from 30A to 10A. The entire test procedure occurs within 20ms, significantly smaller than the mechanical time constant, allowing the influence of the speed variation being ignored during the dynamic test.

In general, it is evident that the coupling between i_d and i_q is well eliminated with the inclusion of the feedforward controller, while slight coupling occurs with too large feedforward gain or closed-loop gain.

Comparing Fig. 13(a) and (b) with K varying from 0.2 to 0.05, the rising time and steady current ripple of the two waveforms are almost identical. Thus, it is evident that the dynamic and static responses of the system are independent of the closed loop gain K .

By comparison of Fig. 13(b) and (c), it can be observed that the dynamic response is closely related to the feedforward gain K_f . As K_f rising from 0.1 to 0.2, the rising times of both steps are reduced by twice. However, overshooting and coupling occur at the second step, which results from the voltage saturation caused by the excessive feedforward gain.

C. Robustness Validation

To validate the robustness of the proposed current control strategy, this section conducts a comprehensive investigation into a wide range of control parameter mismatches. The control parameters are primarily determined by three coefficients corresponding to the plant parameters, denoted as

$$\delta = e^{-\frac{R}{L_1+L_2}T}, \quad \lambda \approx \frac{T_s}{L_1+L_2}, \quad \omega_{res} = \sqrt{\frac{L_1+L_2}{L_1L_2C}} \quad (39)$$

Three sets of experiments are performed conducted with varying parameter mismatches in the digital controller. All test

conditions, along with different parameter variations, are detailed in TABLE II, presented in per-unit values. The experimental results for each condition are illustrated in Fig. 14 with corresponding letter sequence numbers.

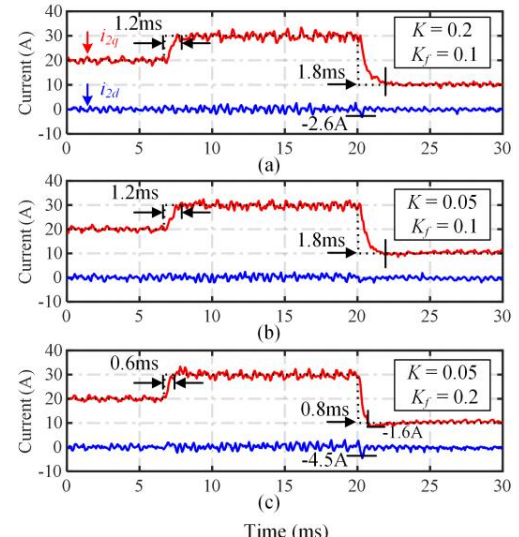


Fig. 13 Dynamic performance with gain variation. (a) $K = 0.2, K_f = 0.1$ (b) $K = 0.05, K_f = 0.1$ (c) $K = 0.05, K_f = 0.2$.

In general, the system is stable in all test conditions. The steady performances of all test conditions are nearly consistent. Additionally, a comparison of the steady current ripple of i_{2q} between 30A and 10A reveals a significantly higher ripple at 30A, while the motor speed remains nearly unchanged during dynamic response. This observation suggests that steady current ripple is primarily induced by measurement noise, which intensifies with increased power.

The first set of experiments, labeled as test 1, evaluates robustness with coefficient δ variation, with R ranging from 0.3 to 3 times its real value. The variation of δ directly impacts the accuracy of zero pole cancellation in the inverse-based controller, potentially affecting the decoupling performance of the controller.

TABLE II
TEST CONDITIONS

	R^*	L_1^*	L_2^*	C^*	f_{res}^*	$\ln(\delta^*)$	λ^*
Test 1	(a) 0.3	1	1	1	1	0.3	1
	(b) 0.5	1	1	1	1	0.5	1
	(c) 2	1	1	1	1	2	1
	(d) 3	1	1	1	1	3	1
	(e) 1	1	1	0.3	1.8	1	1
Test 2	(f) 1	1	1	0.5	1.4	1	1
	(g) 1	1	1	2	0.7	1	1
	(h) 1	1	1	3	0.58	1	1
	(i) 1	0.3	0.3	1	1.8	3.33	3.33
Test 3	(j) 1	0.5	0.5	1	1.4	2	2
	(k) 1	2	2	1	0.7	0.5	0.5
	(l) 1	3	3	1	0.58	0.33	0.33

> REPLACE THIS LINE WITH YOUR MANUSCRIPT ID NUMBER (DOUBLE-CLICK HERE TO EDIT) <

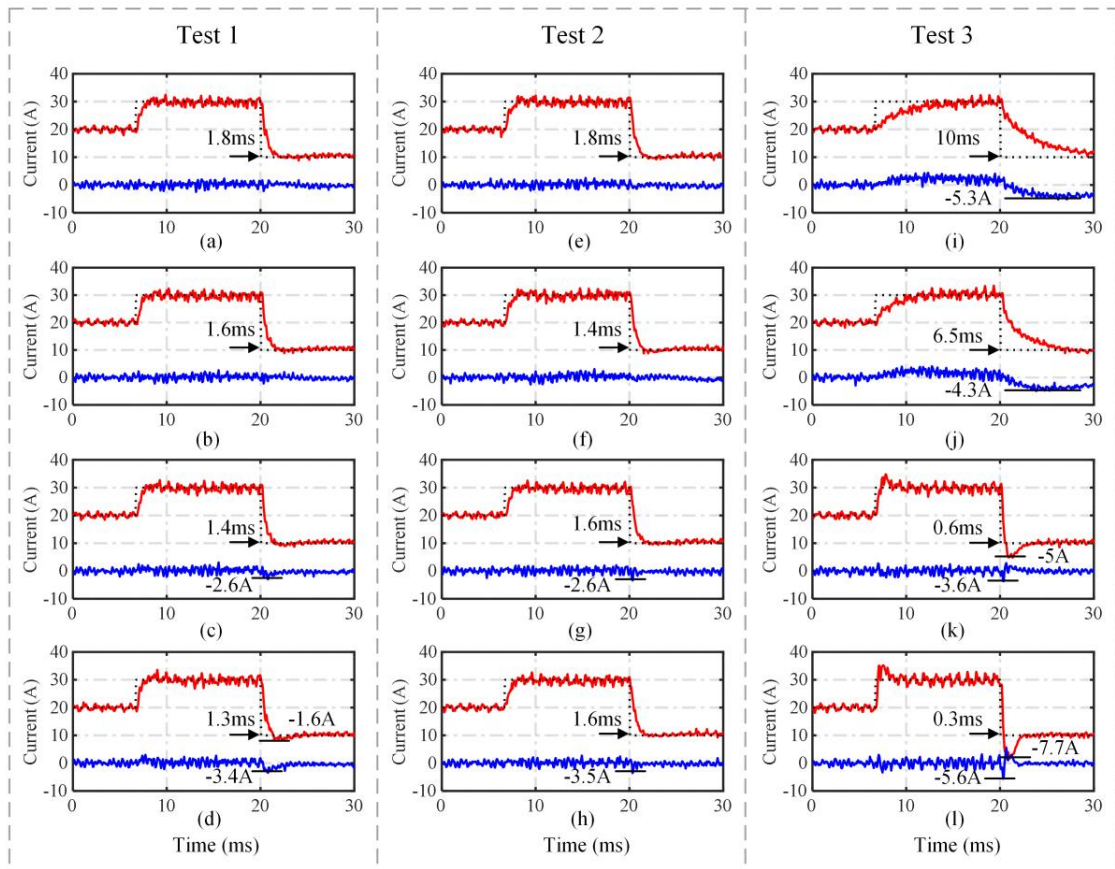


Fig. 14 Dynamic response of proposed methods with different parameter variation

Upon analyzing the dynamic response in test 1, it is evident that dynamic performance is marginally influenced by variations in δ . When the control parameter R is smaller than its actual value, the dynamic performance appears unaffected. However, as R exceeds the actual value, coupling gradually emerges, indicating the sensitivity of the system to higher values of R .

In test 2, the robustness with coefficient ω_{res} variation was assessed, with the filter capacitor C ranging from 0.3 to 3 times its actual value. In the controller design, the resonance frequency ω_{res} primarily determines the phase lag value of the phase compensator. Therefore, the dynamic and steady performance is minimally affected by the mismatch of ω_{res} , as long as the system remains stable. This inference is validated by the experimental results. In test 2, the current response remains nearly unchanged when the capacitor C is smaller than its actual value. A slight coupling is observed when C exceeds its actual value, likely caused by the reduction in phase margin.

Lastly, in test 3, robustness with variations in all three parameters was evaluated, with inductors L_1 and L_2 simultaneously ranging from 0.3 to 3 times of their actual values. As demonstrated in previous results, the variations of δ and ω_{res} have a negligible influence on control performance. However, the variation in λ may yield different outcomes. Since λ is directly in series with the closed-loop gain K , which will further impact the decoupling capability of the

feedforward controller.

The experimental results are consistent with the analysis. In test 3, when L_1 and L_2 are smaller than their actual values, the dynamic response significantly deteriorates, and substantial coupling occurs, primarily resulting from low equivalent closed-loop gain. Conversely, when L_1 and L_2 exceed their actual values, the dynamic response markedly accelerates, achieving a rise time as low as 0.3ms at a 3-times parameter variation, accompanied by significant overshoots and coupling.

In conclusion, the proposed methods exhibit robustness across a broad range, with all parameters varying from 0.3 to 3 times their actual values. The control performance of the proposed methods demonstrates insensitivity to variations in winding resistance R and the filter capacitor C , while showing relatively greater sensitivity to variations in the sum of L_1 and L_2 due to changes in the equivalent closed-loop gain.

VII. CONCLUSION

This paper identifies the influence of the potential negative resonance frequency of the LCL -HSPMSM system within the synchronous rotating frame, which has been typically overlooked in previous studies. Building on this analysis, a robust 2DOF current control strategy is proposed. As the main contribution, a phase gain is introduced to achieve the maximum global stability margin. And the additional coupling caused by the phase gain is addressed by a feedforward

> REPLACE THIS LINE WITH YOUR MANUSCRIPT ID NUMBER (DOUBLE-CLICK HERE TO EDIT) <

controller. Finally, the strong robustness against parameter mismatches is achieved with satisfactory dynamic performance. Theoretical analysis and experimental verification show that the system with proposed control strategy can maintain stability within all the parameters varying from 0.3 to 3 times of the nominal values.

REFERENCES

- [1] J. Dannehl, C. Wessels, and F. W. Fuchs, "Limitations of Voltage-Oriented PI Current Control of Grid-Connected PWM Rectifiers With LCL Filters," *IEEE Transactions on Industrial Electronics*, vol. 56, no. 2, pp. 380–388, Feb. 2009, doi: 10.1109/TIE.2008.2008774.
- [2] W. Wu, Y. Liu, Y. He, H. S.-H. Chung, M. Liserre, and F. Blaabjerg, "Damping Methods for Resonances Caused by LCL-Filter-Based Current-Controlled Grid-Tied Power Inverters: An Overview," *IEEE Transactions on Industrial Electronics*, vol. 64, no. 9, pp. 7402–7413, Sep. 2017, doi: 10.1109/TIE.2017.2714143.
- [3] S. Zhang, S. Jiang, X. Lu, B. Ge, and F. Z. Peng, "Resonance Issues and Damping Techniques for Grid-Connected Inverters With Long Transmission Cable," *IEEE Trans. Power Electron.*, vol. 29, no. 1, pp. 110–120, Jan. 2014, doi: 10.1109/TPEL.2013.2253127.
- [4] Guoqiao Shen, Xuancui Zhu, Jun Zhang, and Dehong Xu, "A New Feedback Method for PR Current Control of LCL-Filter-Based Grid-Connected Inverter," *IEEE Trans. Ind. Electron.*, vol. 57, no. 6, pp. 2033–2041, Jun. 2010, doi: 10.1109/TIE.2010.2040552.
- [5] C. Citro, P. Siano, and C. Cecati, "Designing Inverters' Current Controllers With Resonance Frequencies Cancellation," *IEEE Trans. Ind. Electron.*, vol. 63, no. 5, pp. 3072–3080, May 2016, doi: 10.1109/TIE.2016.2516507.
- [6] Y. He, X. Wang, D. Pan, X. Ruan, and G. Su, "An Ignored Culprit of Harmonic Oscillation in LCL-Type Grid-Connected Inverter: Resonant Pole Cancelation," *IEEE Trans. Power Electron.*, vol. 36, no. 12, pp. 14282–14294, Dec. 2021, doi: 10.1109/TPEL.2021.3084810.
- [7] S. G. Parker, B. P. McGrath, and D. G. Holmes, "Regions of Active Damping Control for LCL Filters," *IEEE Transactions on Industry Applications*, vol. 50, no. 1, pp. 424–432, Jan. 2014, doi: 10.1109/TIA.2013.2266892.
- [8] Chenlei Bao, Xinbo Ruan, Xuehua Wang, Weiwei Li, Donghua Pan, and Kailei Weng, "Step-by-Step Controller Design for LCL-Type Grid-Connected Inverter with Capacitor-Current-Feedback Active-Damping," *IEEE Trans. Power Electron.*, vol. 29, no. 3, pp. 1239–1253, Mar. 2014, doi: 10.1109/TPEL.2013.2262378.
- [9] D. Pan, X. Ruan, C. Bao, W. Li, and X. Wang, "Capacitor-Current-Feedback Active Damping With Reduced Computation Delay for Improving Robustness of LCL-Type Grid-Connected Inverter," *IEEE Transactions on Power Electronics*, vol. 29, no. 7, pp. 3414–3427, Jul. 2014, doi: 10.1109/TPEL.2013.2279206.
- [10] X. Wang, F. Blaabjerg, and P. C. Loh, "Virtual RC Damping of LCL-Filtered Voltage Source Converters With Extended Selective Harmonic Compensation," *IEEE Transactions on Power Electronics*, vol. 30, no. 9, pp. 4726–4737, Sep. 2015, doi: 10.1109/TPEL.2014.2361853.
- [11] Y. He, X. Wang, X. Ruan, D. Pan, X. Xu, and F. Liu, "Capacitor-Current Proportional-Integral Positive Feedback Active Damping for LCL-Type Grid-Connected Inverter to Achieve High Robustness Against Grid Impedance Variation," *IEEE Trans. Power Electron.*, vol. 34, no. 12, pp. 12423–12436, Dec. 2019, doi: 10.1109/TPEL.2019.2906217.
- [12] J. Dannehl, F. W. Fuchs, and P. B. Thøgersen, "PI State Space Current Control of Grid-Connected PWM Converters With LCL Filters," *IEEE Transactions on Power Electronics*, vol. 25, no. 9, pp. 2320–2330, Sep. 2010, doi: 10.1109/TPEL.2010.2047408.
- [13] Z. Zhu, J. Deng, H. Ouyang, and X. Dou, "Optimized Sampling Mechanism for Full-State Feedback Current Control of LCL-Equipped High-Speed PMSMs for Fuel Cell Air Compressor," *IEEE Transactions on Transportation Electrification*, vol. 9, no. 2, pp. 3386–3397, Jun. 2023, doi: 10.1109/TTE.2022.3218153.
- [14] J. Kukkola, M. Hinkkanen, and K. Zenger, "Observer-Based State-Space Current Controller for a Grid Converter Equipped With an LCL Filter: Analytical Method for Direct Discrete-Time Design," *IEEE Transactions on Industry Applications*, vol. 51, no. 5, pp. 4079–4090, Sep. 2015, doi: 10.1109/TIA.2015.2437839.
- [15] C. Cheng, S. Xie, Q. Qian, J. Lv, and J. Xu, "Observer-Based Single-Sensor Control Schemes for LCL-Filtered Grid-Following Inverters," *IEEE Transactions on Industrial Electronics*, vol. 70, no. 5, pp. 4887–4900, May 2023, doi: 10.1109/TIE.2022.3189070.
- [16] J. Zhou, Y. Yao, Y. Huang, and F. Peng, "Motor Current Feedback-Only Active Damping Controller With High Robustness for LCL-Equipped High-Speed PMSM," *IEEE Transactions on Power Electronics*, pp. 1–11, 2023, doi: 10.1109/TPEL.2023.3261447.
- [17] J. Dannehl, M. Liserre, and F. W. Fuchs, "Filter-Based Active Damping of Voltage Source Converters With \$LCLS Filter," *IEEE Trans. Ind. Electron.*, vol. 58, no. 8, pp. 3623–3633, Aug. 2011, doi: 10.1109/TIE.2010.2081952.
- [18] J. Wang, J. D. Yan, L. Jiang, and J. Zou, "Delay-Dependent Stability of Single-Loop Controlled Grid-Connected Inverters with LCL Filters," *IEEE Transactions on Power Electronics*, vol. 31, no. 1, pp. 743–757, Jan. 2016, doi: 10.1109/TPEL.2015.2401612.
- [19] W. Yao, Y. Yang, X. Zhang, F. Blaabjerg, and P. C. Loh, "Design and Analysis of Robust Active Damping for LCL Filters Using Digital Notch Filters," *IEEE Transactions on Power Electronics*, vol. 32, no. 3, pp. 2360–2375, Mar. 2017, doi: 10.1109/TPEL.2016.2565598.
- [20] Y. Yao, Y. Huang, F. Peng, J. Dong, and Z. Zhu, "Discrete-Time Dynamic-Decoupled Current Control for LCL-Equipped High-Speed Permanent Magnet Synchronous Machines," *IEEE Trans. Ind. Electron.*, vol. 69, no. 12, pp. 12414–12425, Dec. 2022, doi: 10.1109/TIE.2021.3127051.
- [21] Y. Yao, Y. Huang, F. Peng, J. Dong, and Z. Zhu, "A General Single-Sensor Damping Framework for LCL-Equipped High-Speed PMSM Drives," *IEEE Transactions on Industrial Electronics*, vol. 70, no. 5, pp. 5375–5380, May 2023, doi: 10.1109/TIE.2022.3186342.
- [22] Y. Yao, Y. Huang, F. Peng, J. Dong, and Z. Zhu, "Dynamic-Decoupled Active Damping Control Method for Improving Current Transient Behavior of LCL-Equipped High-Speed PMSMs," *IEEE Transactions on Power Electronics*, vol. 37, no. 3, pp. 3259–3271, Mar. 2022, doi: 10.1109/TPEL.2021.3109157.
- [23] M. A. Awal, L. Della Flora, and I. Husain, "Observer Based Generalized Active Damping for Voltage Source Converters With LCL Filters," *IEEE Trans. Power Electron.*, vol. 37, no. 1, pp. 125–136, Jan. 2022, doi: 10.1109/TPEL.2021.3093504.
- [24] H. Kim, M. W. Degner, J. M. Guerrero, F. Briz, and R. D. Lorenz, "Discrete-Time Current Regulator Design for AC Machine Drives," *IEEE Transactions on Industry Applications*, vol. 46, no. 4, pp. 1425–1435, Jul. 2010, doi: 10.1109/TIA.2010.2049628.
- [25] A. G. Yepes, F. D. Freijedo, J. Doval-Gandoy, Ó. López, J. Malvar, and P. Fernandez-Comeña, "Effects of Discretization Methods on the Performance of Resonant Controllers," *IEEE Transactions on Power Electronics*, vol. 25, no. 7, pp. 1692–1712, Jul. 2010, doi: 10.1109/TPEL.2010.2041256.
- [26] F. Briz, M. W. Degner, and R. D. Lorenz, "Analysis and design of current regulators using complex vectors," *IEEE Transactions on Industry Applications*, vol. 36, no. 3, pp. 817–825, May 2000, doi: 10.1109/28.845057.